www.ptcer.pl/mccm

MATERIAŁY CERAMICZNE /CERAMIC MATERIALS/, 62, 4, (2010), 442-448

Coupled Microstructural and Transport Effects in *p*-type Perovskites for Hydrocarbon Sensing

K. Darcovich*, J.J. Tunney, M.L. Post

National Research Council of Canada, Institute for Chemical Process and Environmental Technology
1200 Montreal Rd., Ottawa, Ontario, Canada, K1A 0R6
*e-mail: ken.darcovich@nrc-cnrc.gc.ca

Abstract

The chemical gas sensor system of propane (C_3H_8) and propene (C_3H_6) detection in a $SrTi_{0.8}Fe_{0.2}O_3$ matrix was considered. A model was formulated which incorporated the coupled processes of gases diffusing into a porous ceramic and then participating in two chemical reactions: a reversible oxygen adsorption and a two-step surface reaction which consumed the target gas. Microstructural properties of the sensor matrix were coupled with the diffusion and surface chemistry processes. The base state of the electroceramic material was determined through the solution of its equilibrium defect chemistry.

This simulation represents a modeling advance as it is the first to couple spatial variation of microstructural properties with diffusing gas species and the attendant surface chemistry and electroceramic properties, to predict sensor response as a function of film thickness and morphology. The results presented here compare well with experimental measurements over a broad range of conditions. This model validation will be a useful design tool for ensuing materials research work towards improved sensor device development.

Keywords: Perovskite, Hydrocarbon sensing, Propane, Propene, Modeling

POŁĄCZONE EFEKTY MIKROSTRULTURALNY I TRANSPORTOWY W PEROWSKITACH TYPU *p* W PRZYPADKU WYKRYWANIA WĘGLOWODORÓW

Rozpatrzono układ chemicznego czujnika gazu przeznaczonego do wykrywania propanu (C_3H_8) i propenu (C_3H_6) w matrycy $SrTi_{0.8}Fe_{0.2}O_3$. Opracowano model, który uwzględnia połączone procesy dyfuzji gazów do porowatej ceramiki i następnie ich uczestnictwa w dwóch reakcjach chemicznych: odwracalnej adsorpcji tlenu i dwuetapowej reakcji powierzchniowej zużywającej docelowy gaz. Właściwości mikrostrukturalne matrycy czujnika połączono z procesami dyfuzji i chemii powierzchni. Stan podstawowy materiału elektroceramicznego określono w drodze rozwiązania chemii jego defektów równowagowych.

Przedstawiona symulacja stanowi postęp w modelowaniu, ponieważ po raz pierwszy połączono przestrzenne zmiany właściwości mikrostrukturalnych z dyfuzją gazów i związaną z tym chemią powierzchni i właściwościami elektroceramicznymi, aby przewidywać odpowiedź czujnika jako funkcję grubości warstwy i jej morfologii. Zaprezentowane tu wyniki pasują dobrze do pomiarów doświadczalnych przeprowadzonych w szerokim zakresie warunków. Zatwierdzenie tego modelu dostarczy pożytecznego narzędzia do projektowania w przypadku następnych prac badawczych nad materiałami zmierzającymi do rozwoju polepszonych czujników.

Słowa kluczowe: perowskit, wykrywanie węglowodorów, propan, propen, modelowanie

1. Introduction

In connection with increasingly stringent environmental regulations, along with continued efforts to increase fuel efficiency, the role of sensors for either signalling purposes or active feedback has grown significantly more relevant. An important case is that of hydrocarbon sensing in internal combustion engines, requiring robust behaviour in a wide range of operating conditions. Conventional *n*-type metal oxide sensors have consistently exhibited difficulty in providing consistent output under varying humidity, are highly subject to cross-contamination and have demonstrated drifting base values over extended time periods [1, 2].

Additionally, in a reducing environment, the resistance of an *n*-type oxide will tend towards a very low value as the concentration of the reducing species increases. This can lead to a poorly designed signal measurement at higher gas analysis concentrations. For *p*-type oxides, however, higher reducing species concentrations result in higher resistances, a condition which can more readily be accommodated in the associated control circuitry.

In response to the above cited shortcomings, *p*-type semiconductors have been shown to be robust and effective gas sensors, with comparatively better selectivity and stability [3].

Despite these findings, the development and refinement of *p*-type materials as gas sensors has been slow. A number

of *p*-type perovskite oxides exhibit much smaller temperature dependencies of conduction compared to *n*-type semiconducting oxides. The reason for this is related to the oxygen non-stoichiometry of many perovskites, whose effect tends to counteract the thermal promotion of charge carriers [4-7].

Recent studies have identified *p*-type semiconducting perovskites for gas sensing applications, namely $SrTi_{1-x}Fe_xO_3$, which shows good catalytic activity compared to *n*-type sensors [8]. Further, a model based on a diffusion-reaction process was proposed in order to describe the underlying sensing mechanism [9].

The present contribution presents a refinement of the modeling treatment of hydrocarbon sensing with the material $SrTi_{0.8}Fe_{0.2}O_3$, advancing the suite of reactions responsible for its electroceramic response, as well offering a fully coupled and more in-depth analysis of the effects that the ceramic microstructure have on the diffusion and reaction components of the overall system behaviour.

2. Model formulation

The behaviour of the sensing system for propane in Fe-doped strontium titanate is defined by the conducting state of the ceramic, which varies in response to the local concentration of analyte. The conductivity of $SrTi_{0.8}Fe_{0.2}O_3$ has been shown to be primarily dependent its the bulk hole concentration, $[h^{\bullet}]$, [9]. A base state of conductivity can be determined from equilibrium values of hole concentration by applying mass action laws to the system of defect chemistry relations for $SrTi_{0.8}Fe_{0.2}O_3$ [10].

2.1. Defect chemistry of Fe-doped $SrTiO_3$

For an equilibrium state in air, the following chemical reactions define the defect chemistry:

– The reversible incorporation of the gas phase oxygen:

$$\frac{1}{2}O_2 + V_{O,surf}^{\bullet\bullet} \underset{k_{red}}{\overset{k_{ox}}{\rightleftharpoons}} O_{O,surf}^{x} + 2h^{\bullet}. \quad (1)$$

– Holes are in balance with electrons according to

$$\varnothing \rightleftharpoons e' + h^{\bullet}. \quad (2)$$

– Further, local concentrations of holes affect the ionic composition of the iron in the ceramic according to

$$Fe^{4+} \underset{k_{Fe_r}}{\overset{k_{Fe_f}}{\rightleftharpoons}} Fe^{3+} + h^{\bullet}. \quad (3)$$

A kinetic study, allowing a determination of the forward pre-exponential rate constant for the term k_{Fe_f} in Eq. 3 was published by Østdal *et al.* [11]. The activation energy for this reaction was discussed in [12].

Using a mass action law approach, an equilibrium suite of species concentrations can be determined. Eqs. 1 through 3 are linked to mass action constants given in Eq. 4. In these expressions, as well as with rate calculations, the concentration of near-surface oxygen $O_{O,surf}^{x}$, is considered to be invariant, and is thus incorporated into the rate coefficients and mass actions constants [9], shown below:

$$K_1 = \frac{[h^{\bullet}]^2}{[V_{O,surf}^{\bullet\bullet}]\sqrt{pO_2}},\ K_2 = [e'][h^{\bullet}]^2,\ K_3 = \frac{[Fe^{3+}][h^{\bullet}]}{[Fe^{4+}]}. \quad (4)$$

To allow for the equilibrium concentrations of five species to be determined, two other relations are invoked. The electroneutrality condition requires that

$$2[V_{O,surf}^{\bullet\bullet}] + [h^{\bullet}] = [Fe^{3+}] + [e']. \quad (5)$$

The mass conservation of iron can be expressed with $[Fe_{total}]$ known from the stoichiometric level of iron doping in the strontium titanate, calculated as a concentration. Thus,

$$[Fe_{total}] = [Fe^{3+}] + [Fe^{4+}]. \quad (6)$$

Table 1 also lists the values of the Arrhenius-type constants for the reactions shown in Eqs.1 through 3, as well as the mass action constants given in Eqs. 4 [12]. For a given reaction, the kinetic coefficient, k_i (for reaction *i*), would be expressed as, $k_i = k_{0,i} \exp(-E_{act,i}/RT)$. Solution of the system of Eqs. 1 through 6 across a range of temperatures for an oxygen partial pressure (pO_2) of 20 kPa and an iron-doping stoichiometric value of ν_{Fe} = 0.2 yields the curve in Fig. 1, which matches results from Denk *et al*. [13].

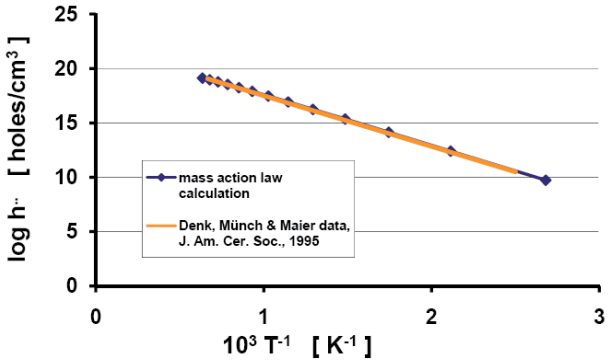

Fig. 1. Validation of defect chemistry solution algorithm, compared with published results [13]. Parameters are pO_2 = 20 kPa and ν_{Fe} = 0.2.

2.2. Effect of target gas

The sensing functionality arises from the introduction of a target gas into the system, and its subsequent alteration

Table 1. Kinetic parameters for the reactions occurring in the C_3H_8 - $SrTi_{0.8}Fe_{0.2}O_3$ system, where k_0 is the pre-exponential constant, and E_{act} [kJ/mol] is the activation energy for each case. Above, R is the gas constant of 8.314 [J/mol·K], and T is the temperature in [K].

units	K_1 $\left[\frac{mol}{m^3\cdot\sqrt{Pa}}\right]$	K_2 $\left[\frac{mol^2}{m^6}\right]$	K_3 $\left[\frac{mol}{m^3}\right]$	k_{red} $\left[\frac{m^3}{mol\cdot s}\right]$	k_{ox} $\left[\frac{1}{s\cdot\sqrt{Pa}}\right]$	k_{Fe_f} $\left[\frac{1}{s}\right]$	k_{Fe_r} $\left[\frac{m^3}{mol\cdot s}\right]$	k_{redox} $\left[\frac{m^9}{mol^2\cdot kg\cdot s}\right]$
k_0	1.81×10^{-9}	4.34×10^{-15}	1.41×10^{-15}	9.66×10^{5}		7.04×10^{10}		575.0
E_{act}	159.2	$\frac{318.4-0.058T}{RT}$	113.9	100.0		77.2		56.9
f[n]					$k_{red}\cdot K_1$		k_{Fe_f}/K_3	

of the defect chemistry equilibrium. In the present case, propane and propene are considered as target gases. The net reactions of propane and propene with the semiconducting bulk of the $SrTi_{0.8}Fe_{0.2}O_3$ are given as [14]:

$$\begin{aligned} C_3H_8 + 10\,O^x_{O,surf} + 20\,h^\bullet &\xrightarrow{k_{redox}} 10\,V^{\bullet\bullet}_{O,surf} + 4H_2O + 3CO_2, \\ C_3H_6 + 9\,O^x_{O,surf} + 18\,h^\bullet &\xrightarrow{k_{redox}} 9\,V^{\bullet\bullet}_{O,surf} + 3H_2O + 3CO_2\,. \end{aligned} \quad (7)$$

The diffusion and reaction of analyte inside the ceramic microstructure serves to reduce the hole concentration by consumption of the surface oxygen, thereby altering the electroceramic material properties. The bulk conductivity of the material changes in relation to the presence and quantity of analyte, hence the hydrocarbon sensing functionality of $SrTi_{0.8}Fe_{0.2}O_3$. It was observed over preliminary trials that the mechanisms as expressed in Eq. 7 produced a disparity when calculating $[h^\bullet]$ values. Introduction of the target gas species overestimated the $[h^\bullet]$ reduction. This inconsistency was also noted in [9]. To provide a more coherent context, it is proposed that the overall reactions expressed in Eq. 7, be re-expressed in two distinct steps with different kinetic coefficients. The two steps include an adsorption reaction and an oxidation reaction, that proceed at appreciably different rates:

$$\begin{aligned} C_3H_8 + O^x_{O,surf} &\xrightarrow{k_{R,ads}} C_3H_8{-}O^x_{O,surf}, \\ C_3H_8{-}O^x_{O,surf} + 9\,O^x_{O,surf} + 20\,h^\bullet &\xrightarrow{k_{R,ox}} 10\,V^{\bullet\bullet}_{O,surf} + 4H_2O + 3CO_2, \\ C_3H_6 + O^x_{O,surf} + &\xrightarrow{k_{R,ads}} C_3H_6{-}O^x_{O,surf}, \\ C_3H_6{-}O^x_{O,surf} + 8\,O^x_{O,surf} + 18\,h^\bullet &\xrightarrow{k_{R,ox}} 9\,V^{\bullet\bullet}_{O,surf} + 3H_2O + 3CO_2\,. \end{aligned} \quad (8)$$

It has been observed that the kinetic parameters for adsorption component of the reactions listed in Eq. 8 corresponded to the concentration profiles of C_3H_8 and C_3H_6 inside the ceramic microstructure, as per the analytical approach first presented by Sakai *et al.* [9, 15]. These same kinetic parameters cannot also correctly predict the observed sensor response, hence the reaction scheme was is expanded to two steps. The kinetic parameters for the oxidation step were determined from averaging equilibrium data across a concentration range for the analyte hydrocarbons, represented by generic species *R*, according to

$$[R_{ads}] = \frac{S \cdot k_{R,ads}[R]}{k_{R,ox}[h^\bullet]^2}, \quad (9)$$

where *S* is the fraction of available adsorption sites.

Table 2. Kinetic parameters for the reactions occurring in the C_3H_8 - $SrTi_{0.8}Fe_{0.2}O_3$ system. These parameters apply directly to 1.5 μm diameter particles.

units	$k_{0,R,ads}$ $\left[\frac{m^9}{mol^2 \cdot kg \cdot s}\right]$	$E_{R,ads}$ $\left[\frac{kJ}{mol}\right]$	$k_{0,R,ox}$ $\left[\frac{m^9}{mol^2 \cdot kg \cdot s}\right]$	$k_{0,R,ox}$ $\left[\frac{kJ}{mol}\right]$
R = C_3H_8	575.0	56.9	57.5	56.9
R = C_3H_6	6.582×10^8	32.0	2.03	32.0

Values of the kinetic parameters for the two step reaction are given in Table 2. As explained in [9], the $k_{0,R,ox}$ values were obtained from kinetic measurements, and need to be adjusted by the apparent density of the gas phase in kg/m^3, $\rho_{apparent} = \rho_{bulk}(1 - \varepsilon)$, for consistency with the material transport treatment. It can be seen that values of $E_{R,ads}$ and $E_{R,ox}$ were assigned to be the same. While clearly hypothetical, the modeling was done this way in the interest of retaining the existing temperature functionality and allowing for different kinetic rates. More precise kinetic parameters for these reactions will require experimental work.

2.3. Microstructural properties

The physical domain under consideration is a layer of grain-based sintered $SrTi_{0.8}Fe_{0.2}O_3$ of 10 μm thickness. For comparison purposes, a system considered in [9] was adopted here. The films were prepared with powders prepared by solid state reaction for 1.5 μm grain sizes, while other films were made with ultra-fine 70 nm diameter grains, which were sol precipitated powders sintered in air. Relevant physical parameters are, particle size $d_p = 1.5\times10^{-6}$ m, pore radius, $r_p = 7.5\times10^{-7}$ m, porosity $\varepsilon = 0.30$, film thickness = 10 μm and the $SrTi_{0.8}Fe_{0.2}O_3$ solid density $\rho = 5160$ kg/m^3. Further, the parameter estimation incorporated a particle size functionality, whereby, the kinetic coefficients are multiplied by an area factor a_F, set equal to unity for the base case of 1.5 μm diameter particles. Kinetic data was available for two particle diameters, 1.5 μm and 0.07 μm and a surface factor (Eq. 19 in reference [9]) served to correct the kinetics for different grain sizes. In the present analysis, a regression analysis was done that produced a function given in Eq. 10 which gave the kinetic rates as a smooth function of grain diameter, as well as exactly interpolating the grain diameters with measured values. The relation was found to be

$$a_F = 1.2853 \cdot \left(10^6 \cdot d_p\right)^{-0.619}, \quad (10)$$

where d_p is the particle diameter, expressed in [m].

2.4. Gas transport

The sensing function arises from the diffusion of the hydrocarbon target gas into the porous ceramic layer, and its subsequent chemical interaction with the bulk of the microstructure. The two competing processes of diffusion and reaction produce concentration profiles of the relevant chemical species within the microstructure, thereby determining the spatial distribution of properties which contribute the overall measured conductivity of a sensor device.

To define species diffusivity through the film, Knudsen diffusion is used because of the small pore sizes which occur with particles in the size range considered [15, 16]. The following expression is used to calculate the Knudsen diffusivity for all gases locally throughout the domain:

$$D_{k_i} = \frac{\varepsilon}{\tau}\frac{4r_p}{3}\sqrt{\frac{2RT}{\pi M_i}} \qquad \left[m^2 \cdot s^{-1}\right]. \quad (11)$$

In Eq. 11, ε refers to porosity and τ is the tortuosity [17]. Above, *T* is temperature, M_i the molecular weight of species

i, r_p the pore radius, and R is the gas constant. The sensor operating temperature was set at 673 K or 400°C.

The transport of gas through a porous structure is governed by the convection diffusion equation shown below:

$$\frac{\partial}{\partial t}(\rho C_i) + \nabla \cdot (\rho \vec{\upsilon} C_i) = -\nabla \cdot \vec{J}_i + S_i \cdot \qquad (12)$$

The above equation has a concentration rate term and a convective transport term for species i which is a function of the velocity vector υ, on the right-hand side, as well as the diffusive flux term $J_i = \rho D K_i r C_i$ and the term S_i which is a source term for creation or elimination of target species i. In one dimension, a simplified equation can be considered:

$$D_{K_i} \frac{\partial^2 C_i}{\partial x^2} + \sum \nu_j k_j \prod_{k=1}^{N_j} C_k^{\nu_k} = 0 \cdot \qquad (13)$$

In Eq. 13 for all j reactions which produce or consume species i, ν_j is the stoichiometric coefficient and C_k are the concentrations of the N_j reagents.

Fig. 2. Schematic of computational mesh used in the simulation.

2.5. Numerical implementation

The system was treated on a strip type grid shown in Fig. 2. The upper and lower axial boundaries were treated as symmetry planes, so that the problem was essentially reduced to one dimension. In physical terms, this represents the study of diffusion and chemistry as a function of the depth away from the sensor-gas interface. A film thickness of 10 μm was considered. Air with a molar composition in the mole fractions of $mf_{O_2,0} = 0.2116$ and $mf_{N_2,0} = 0.7884$ was assumed at the sensor-air interface. When target gas is present, it has an interfacial mole fraction, mfR.

The transport equation (Eq. 13) was solved with the following boundary conditions:

$\frac{\partial C_i}{\partial n} = 0$ on axial boundaries and internal boundary,

$$mf_{O_2} = \frac{mf_{O_2,0}}{mf_{O_2,0} + mf_{N_2,0} + mf_R}, \qquad (14)$$

$$mf_{N_2} = \frac{mf_{N_2,0}}{mf_{O_2,0} + mf_{N_2,0} + mf_R}.$$

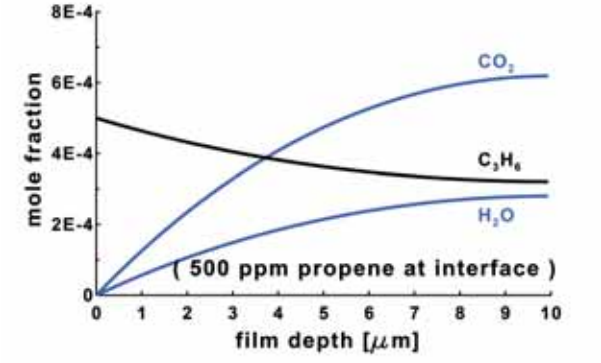

Fig. 3. Concentration profile of propene inside 10 μm thick $SrTi_{0.8}Fe_{0.2}O_3$ layer at 673 K and ε = 0.30.

The solution algorithm consisted of iterating one time on each of the five gas species diffusion equations, then solving for $[h^\bullet]$ in each cell, making use of the rate expression $\partial[h^\bullet]/\partial t = 0$. The other surface species concentrations could then be directly calculated from simple defect chemistry relations.

The model described above was implemented numerically with the open-source software OpenFOAM (Field Operation And Manipulation), which is an object-oriented high level code designed for treating problems which can be represented by partial differential field equations [18].

3. Results and discussion

3.1. Diffusion and reaction

A plot of propene concentration in a 10 μm thick $SrTi_{0.8}Fe_{0.2}O_3$ layer is shown in Fig. 3. The oxygen and nitrogen content is quite large compared to propene, O_2 and H_2O, and as such, their concentration profiles do not vary appreciably. Propane has comparatively slow oxidation kinetics and thus has a concentration profile that is at and essentially equal to the interface concentration.

3.2. Conductivity calculations

Fundamental to sensor behaviour are the material conductivity properties, and the changes which arise upon exposure to analyte gas. Kharton *et al*. [19, 20] addressed the conductivity of a number of strontium based perovskites, among which was $SrTi_{0.8}Fe_{0.2}O_3$. Fig. 6 in [20] shows that the transference number (t_0) at 1250 K for $SrTi_{0.8}Fe_{0.2}O_3$ is less than 0.01. There is an exponential decrease of t_0 as the temperature decreases, such that the ionic conductivity can be considered negligible when considering conductivity. A general expression of conductivity σ can be given as [21]

$$\sigma = e_0 \mu_h [h^\bullet] + \sum z_i e_0 \mu_i [X_i] - e_0 \mu_e [e'], \qquad (15)$$

where e_0 is the elementary charge (1.602176×10^{-19} C), μ_h is the hole mobility, and for each mobile ion, X_i, z_i and μ_i are its respective charge number and mobility, and μ_e is the electron mobility. The electron concentration $[e_0]$ was found to be around 15 orders of magnitude less than $[h^\bullet]$, so the right hand term was neglected in Eq. 15. Further, with $t_0 << 0.01$, the second term in Eq. 15 representing ionic conductivity was also dropped.

As verification of the model, a study of the absolute values of conductivities was undertaken. A temperature dependent empirical expression for μ_h in $SrTi_{0.8}Fe_{0.2}O_3$ is given in [13] as, $\mu_h = 89.0\ T^{-2.36}$. Using values of $[h^\bullet]$ determined by simulation across a range of temperatures, it was used to calculate values of conductivity. In Fig. 4 these values are compared to experimental data from the literature for bulk conductivities of $SrTi_{0.8}Fe_{0.2}O_3$ in air [8, 19]. The calculations match experimental values reasonably well, noting that there were two separate and independent temperature functionalities employed, an empirical one for μ_h and the Arrhenius based set of reaction and diffusion kinetics used to arrive at $[h^\bullet]$ in the simulation. The coherence between the simulated and measured data suggest a general soundness of the physical mechanisms incorporated into the present

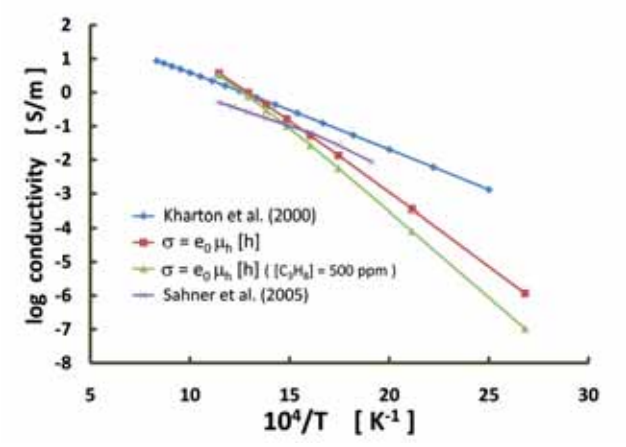

Fig. 4. Conductivity versus temperature plots for bulk $SrTi_{0.8}Fe_{0.2}O_3$ material. Experimental data is compared against fundamentals based calculations from the numerical simulation.

model. Basic conductivity values are known to show high variability in the literature, as many microstructural and atmospheric factors influence the measurement [8, 9].

3.3. Hydrocarbon sensing

For the case of propene as analyte, Fig. 5 shows concentration profiles of the relevant surface species, $h^{\bullet}$, $V_{O,surf}^{\bullet\bullet}$, Fe^{3+} and Fe^{4+} as a function of position across a 10 μm film. In general it is known that the material electrical conductivity, and hence sensor response, is proportional to $[h^{\bullet}]$. It is evident from Fig. 5 that conductivity decreases in the range of 30 to 50 % are produced, which are readily measurable changes. As a function of analyte concentration, Fig. 6 shows very good comparison of simulated results with experimental values. Of note here, is a calculation also plotted in Fig. 6 based on defect chemistry calculations, Eqs. 1 through 6. In the case of propane, the defect chemistry calculation is accurate, since there is little spatial concentration variation of the interacting species across the sensor film.

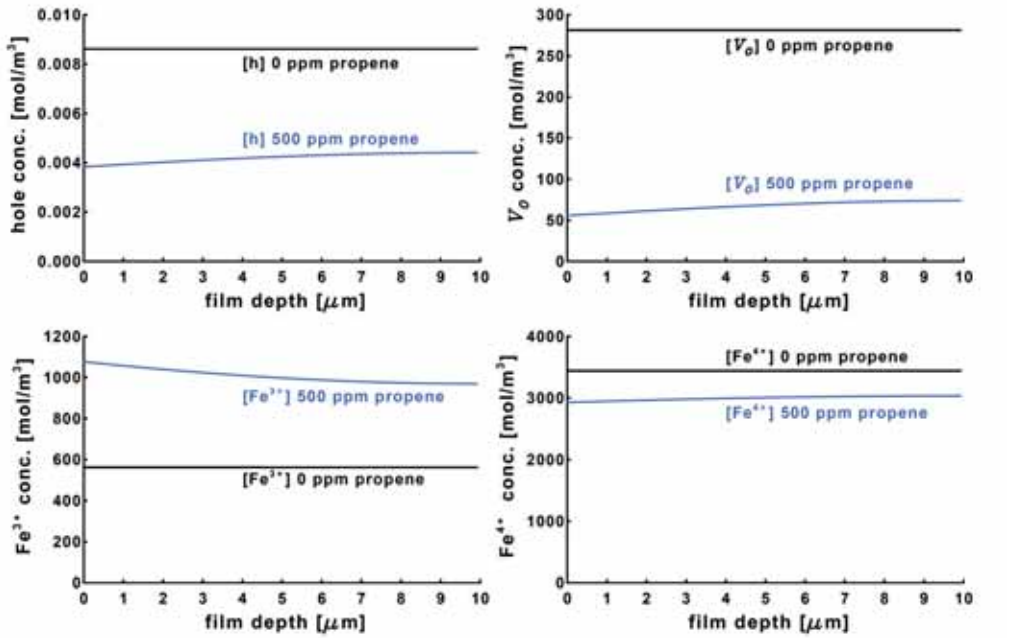

Fig. 5. Concentration profiles of surface species across a 10 μm film, for cases of 0 and 500 ppm propene (C_3H_6) analyte, at 673 K and ε = 0.30.

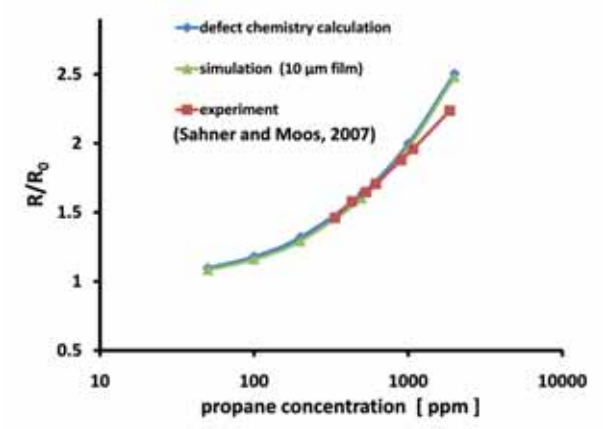

Fig. 6. Integrated simulated R/R_0 values over a 10 μm film, for propane (C_3H_8) analyte as a function of concentration, compared to values from defect chemistry calculations and experimental values from [9]. Simulations run at 673 K and ε = 0.30.

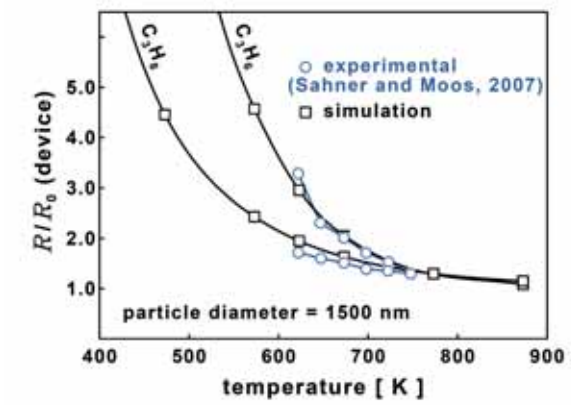

Fig. 7. Integrated R/R_0 values over a 10 μm film, for 500 ppm propane (C_3H_8) and propene (C_3H_6) analytes, for 1500 nm diameter grain sizes at ε = 0.30. The data are compared to experimental values from [9].

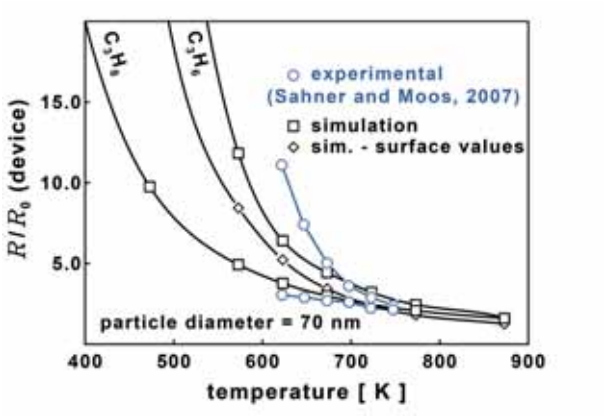

Fig. 8. Integrated R/R_0 values over a 10 μm film, for 500 ppm propane (C_3H_8) and propene (C_3H_6) analytes, for 70 nm diameter grain sizes at ε = 0.30. Also shown are R/R_0 values from the gas phase-sensor material interface simulated with the propene case. The data are compared to experimental values from [9].

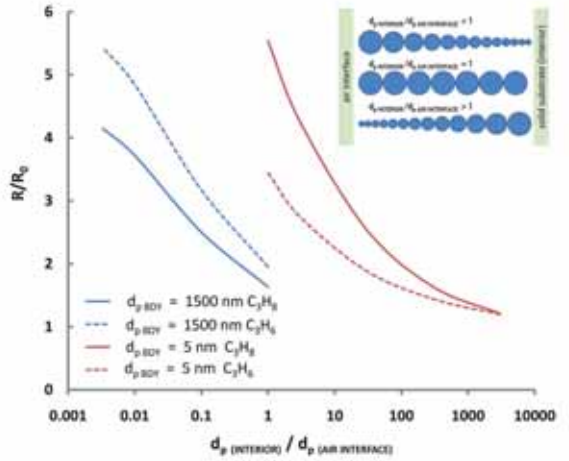

Fig. 9. Integrated R/R_0 values over a 10 μm film with linearly graded grain diameters, for 500 ppm propane (C_3H_8) and propene (C_3H_6) at 673 K and ε = 0.30. The inset is a schematic depiction of the types of grain size gradings considered.

3.4. Microstructural effects

For both C_3H_8 and C_3H_6, sensor response is plotted against temperature for coarse and fine grain sizes, in Figs. 7 and 8. Sahner and Moos [9] employed different kinetic coefficients for different grain sizes in their experiments.

To unify the approach, as well as to provide a means to decouple the adsorption and oxidation steps undergone by the analyte hydrocarbons, the parameter a_F as given in Eq. 10 was employed. The approach was accurate for predicting R/R_0 values for both the 1.5 and 0.07 μm grain diameters considered in Figs. 7 and 8. In Fig. 8 an additional plot is made, showing values of R/R_0 at the gas phase-sensor material interface. As there was significant spatial variation in species concentration profiles across the 10 μm thick sensing layer, R/R_0 values corresponding to the gas phase-sensor material interface were a poorer match to the experimental values when compared to the values integrated over the entire layer. Taking gas phase-sensor material interface R/R_0 values is tantamount to estimating device behaviour purely by defect chemistry calculations, which do not have access to spatially varying species profiles. Recall Fig. 6, where the defect chemistry calculations for the propane case, with essentially at spatial species concentration profiles over 10 μm, were sufficiently accurate.

3.5. Parametric studies

The effect of grading the grain diameters across the 10 μm film are shown in Fig. 9, for propane at 673 K. The data plotted in Fig. 9 assume a linear gradation of grain diameter, beginning at the air-ceramic interface with the boundary diameter d_{P_BDY} given in the legend. The diameter range was from 5 nm to 1500 nm, thus $d_{P\_INTERIOR}$ /$d_{P\_AIR\ INTERFACE}$ values less than 1 are layers with coarser particles at the air interface, while values greater than one represent layers with finer particles at the air interface. In the arrangement with coarse interface grains, the sensor response is enhanced by a graded microstructure, a consequence of the increased interfacial area attributable to including

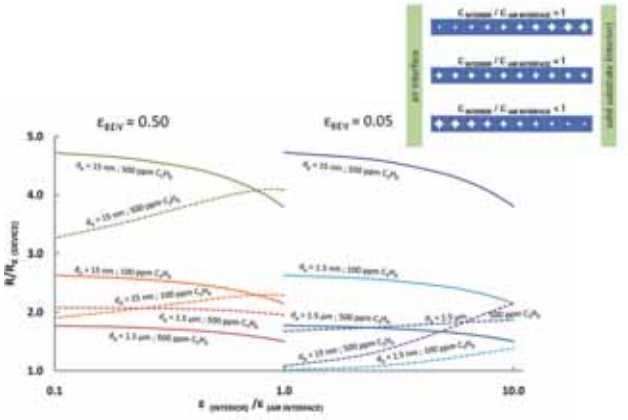

Fig. 10. Integrated R/R_0 values over a 10 μm film for graded microstructure porosities, at different grain diameters and analyte concentrations of propane (C_3H_8) and propene (C_3H_6) at 673 K. The inset is a schematic depiction of the types of porosity gradings considered.

smaller grain sizes, which provides more sites for the surface chemical reactions with the analyte gas. The curves in Fig. 9 serve to illustrate how microstructral manipulation could be employed to enhance selectivity of the sensor for either propane or propene. For example, a microstructure with a coarse-grained interface and graded to finer interior particle diameters improves selectivity for propene. Under most conditions, $SrTi_{0.8}Fe_{0.2}O_3$ has a higher response with propene, but if the grain diameters are reduced to 5 nm, it can be seen that the higher adsorption kinetics of propane give it a higher response in very fine grained microstructures.

Sensor response calculations resulting from grading the porosity across the layer in the range of 0.50 > ε > 0.05 are shown in Fig. 10. For cases with propene, it can be seen that increasing porosity away from the ceramic-air interface improves response, through facilitating diffusion for the system with a comparatively lower surface oxidation rates. As with graded grain sizes, propane selectivity can be enhanced by finding microstructural parameters such as small

grain sizes and a less porous interior of the ceramic layer. Coarser grain sizes are shown to improve the selectivity for propene.

4. Conclusions

A model and simulation based on physical fundamentals has been developed for the gas sensing system of propane and propene detection based on *p*-type conductivity in a layer of $SrTi_{0.8}Fe_{0.2}O_3$. Validation of the model was demonstrated through matching defect chemistry calculations for surface states, as well as making accurate predictions compared to experimental data measured across a range of temperatures and concentrations. Further, basic conductivity values calculated for the diffusion and reaction mechanisms were a close match to experimental data. Accuracy of the results was conserved with a unified treatment where the analyte reactions were expanded to two distinct steps of adsorption and oxidation.

The decoupled reaction mechanisms serve to demonstrate that the sensing of propene gas is more complex, owing to a greater difference in the kinetics of the adsorption and oxidation steps, an electroceramic behaviour that to this point had only been observed experimentally, without mechanistic rationale. The present simulation represents a modeling advance with its coupling of diffusing and reacting gases, with spatially varying surface species profiles determined as a function of local microstructure. This will prove to be a useful design tool for on-going materials research towards improved sensor device development.

References

[1] Meixner H., Lampe U.: „Metal oxide sensors", Sensors and Actuators B, 33, 1-3, (1996), 198-202.

[2] Williams D.E.: „Semiconducting oxides as gas-sensitive resistors", Sensors and Actuators B, 57, 1-3, (1999), 1-16.

[3] Yannopoulos L.N.: „A *p*-type semiconductor thick film gas sensor", Sensors and Actuators, 12, 3, (1987), 263-273.

[4] Moseley P.T.: „Solid State Gas Sensors", Meas. Sci. Technol., 8, 3, (1997), 223-237.

[5] Moseley P.T., Williams D.E.: „Gas sensors based on oxides of early transition metals", Polyhedron, 8, 13-14, (1989), 1615-1618.

[6] Tunney J.J., Post M.L., Du X., Yang D.: „Temperature Dependence and Gas Sensing Response of Conduction for Mixed Conducting $SrFe_yCo_zO_x$ Thin Films", J. Electrochem. Soc., 149, 6, (2002), H113-H118.

[7] Moos R., Menesklou W., Schreiner H.-J., Hardtl K.H.: „Materials for temperature independent resistive oxygen sensors for combustion exhaust gas control", Sensors and Actuators B, 67, 1-2, (2000), 178-183.

[8] Sahner K., Moos R., Matam M., Tunney J.J., Post M.: „Hydrocarbon sensing with thick and thin film *p*-type conducting perovskite materials", Sensors and Actuators B, 108, 1-2, (2005), 102-112.

[9] Sahner K., Moos R.: „Modeling of hydrocarbon sensors based on p-type semiconducting perovskites", Phys. Chem. Chem. Phys., 9, 5, (2007), 635-642.

[10] Maier J., Münch W.: „Chemical transport in mixed conductors: application to the model materials $SrTiO_3$ and ZrO_2", J. Chem. Soc., Faraday Trans., 92, 12, (1996), 2143-2149.

[11] Østdal H., Sörensen G., Daneshvar B., Skibsted L.H.: „Oxidative dimerisation of tyrosine by the hypervalent meat pigment ferrylmyoglobin", Eur. Food Res. Technol., 216, 1, (2003), 23-27.

[12] Merkle R., Maier J.: „Oxygen incorporation into Fe-doped $SrTiO_3$: Mechanistic interpretation of the surface reaction", Phys. Chem. Chem. Phys., 4, 17, (2002), 4140-4148.

[13] Denk I., Münch W., Maier J.: „Partial conductivities in $SrTiO_3$: bulk polarization experiments, oxygen concentration cell measurements, and defect-chemical modeling", J. Am. Cer. Soc., 78, 12, (1995), 3265-3272.

[14] Mahesh M., Kumar M.L., Post: „Effect of grain boundaries on hydrocarbon sensing in Fe-doped p-type semiconducting perovskite $SrTiO_3$ films", J. Appl. Phys., 97, 11, (2005), 114916-(1-8).

[15] Sakai G., Matsunaga N., Shimanoe K., Yamazoe N.: „Theory of gas-diffusion controlled sensitivity for thin film semiconductor gas sensor", Sensors and Actuators B, 80, 2, (2001), 125-131.

[16] Darcovich K., Garcia F.F., Jeffrey C.A., Tunney J.J., Post M.L.: „Coupled microstructural and transport effects in *n*-type sensor response modeling for thin layers", Sensors and Actuators A, 147, 2, (2008), 378-386.

[17] Wijngaarden R.J., Kronberg A., Westerterp K.R.: „Industrial catalysis-optimizing catalysts and processes", Wiley-VCH, Weinheim, 1998.

[18] Powell A.C. IV, Arroyave R.: „Open source software for materials and process modeling", JOM, 60, 5, (2008), 32-39.

[19] Kharton V.V., Viskup A.P., Kovalevsky A.V., Figueiredo F.M., Jurado J.R, Yaremchencko A.A., Naumovich E.N., Frade J.R.: „Surface-limited ionic transport in perovskites $Sr_{0.97}(Ti,Fe,Mg)O_{3-\delta}$", J. Mater. Chem., 10, 5, (2000), 1161-1170.

[20] Kharton V.V., Kovalevsky A.V., Tsipis E.V., Viskup A.P., Naumovich E.N., Jurado J.R., Frade J.R.: „Mixed conductivity and stability of A-site-defficient $Sr(Fe,Ti)O_{3-\delta}$ perovskites", J. Solid State Electrochem., 7, 1, (2002), 30-36.

[21] Côté R: „From Classical Mobility to Hopping Conductivity: Charge Hopping in an Ultracold Gas", Phys. Rev. Lett., 85, 25, (2000), 5316-5319.

♦

Received 30 March 2010; accepted 5 May 2010